Editors' Suggestion

Agility of Spin Hall Nano-Oscillators

F. J. T. Gonçalves,[1,*] T. Hache,[1] M. Bejarano,[1,2] T. Hula,[1,3] O. Hellwig,[1,3] J. Fassbender,[1,2] and H. Schultheiss[1,2]

[1] *Helmholtz-Zentrum Dresden–Rossendorf, Institute of Ion Beam Physics and Materials Research, Bautzner Landstraße 400, Dresden 01328, Germany*

[2] *Technische Universität Dresden, Dresden 01062, Germany*

[3] *Institut für Physik, Technische Universität Chemnitz, Chemnitz 09107, Germany*

(Received 12 March 2021; revised 14 September 2021; accepted 5 November 2021; published 30 November 2021)

We investigate the temporal response of constriction-based spin Hall nano-oscillators driven by pulsed stimuli using time-resolved Brillouin light scattering microscopy. The growth rate of the magnetization auto-oscillations, enabled by spin Hall effect and spin-orbit torque, is found to vary with the amplitude of the input voltage pulses, as well as the synchronization frequency set by an external microwave input. The combination of voltage and microwave pulses allows us to generate auto-oscillation signals with multilevel amplitude and frequency in the time domain. Our findings suggest that the lead time of processes such as synchronization and logic using spin Hall nano-oscillators can be reduced to the nanosecond timescale.

DOI: 10.1103/PhysRevApplied.16.054050

I. INTRODUCTION

Magnetic oscillators are among the most promising means to perform brain-inspired solid-state-based computation [1,2] and microwave communication technologies [3]. These are primarily based on magnetization auto-oscillations (AOs) in the gigahertz frequency range. AOs arise when the Gilbert damping is compensated by the torque transferred from a pure spin or spin-polarized current to the magnetization, due to spin-orbit torque (SOT) or spin-transfer torque [4–8]. Here, the pure spin current is generated via spin Hall effect (SHE) [9,10], in an adjacent nonferromagnetic, metallic layer with large spin Hall angle [11–13]. In recent years, several prototypical oscillator geometries have surfaced, such as spin Hall nano-oscillators (SHNOs) [14–16], the spin torque nano-oscillators [17,18] and nonlocal spin-injection spin valves [19,20]. Often, these are physically arrayed into a network, when synchronization between oscillators [21–23] allows for complex operations, such as pattern recognition [24,25]. To some extent, an isolated magnetic oscillator in itself can mimic a pseudonetwork of oscillators [26,27] if external time-dependent stimuli are applied to exploit its nonlinear response. Thus, an important requisite for a magnetic oscillator is agility, that is, the ability to respond to time-dependent external stimuli in a way that the resulting amplitude, frequency, or phase can be utilized reliably as a processing output.

In this manuscript, we investigate the temporal response of nano-constriction SHNOs driven by voltage pulses and microwave pulses. We find that the growth rate of the AO signal increases with voltage pulse amplitude and that the time delay between the voltage pulse and the AO response is reduced considerably at large pulse amplitudes. AO signals could be obtained using voltage pulses with a duration of a few nanoseconds. Moreover, we discuss how the AO response can be improved by means of injection locking to an external microwave pulse. Furthermore, we demonstrate how the pulsed operation results in a reliable multilevel AO amplitude and frequency in the time domain.

Figure 1(a) shows a top-view scanning electron microscopy (SEM) image of the disk-shaped nanoconstriction SHNO. The two magnetic disks have a radius of 2.6 μm and overlap by approximately 50 nm, resulting in a constriction width of 1.13 μm. The structures are fabricated on a silicon substrate using a resist mask created by electron-beam lithography (EBL), followed by sputtering of the thin-film layers Ta(2 nm)/Pt(7 nm)/$Ni_{81}Fe_{19}$(5 nm)/Ta(2 nm) and liftoff. The electrical contacts are created using an additional EBL resist mask followed by thermal evaporation of the metals (Cr/Au) and liftoff. The structure under test has an average resistance of 350 Ω.

The temporal response of the SHNOs is tested under two types of pulse excitation, as illustrated in Fig. 1(a). The first type concerns the use of voltage pulses (V_p) to drive the AOs and the second type concerns the combined use of voltage and radio frequency pulses (rf_p) in order to

*f.goncalves@hzdr.de

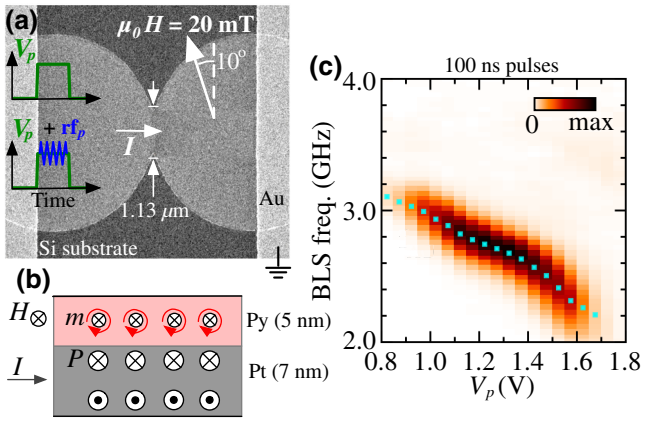

FIG. 1. (a) SEM image of the SHNO and measurement geometry. (b) Schematic illustration of the layer stack indicating the direction of the current (I), the polarization of the pure spin current (P) and the precession induced on the magnetic moment (m) of the Py ($Ni_{81}Fe_{19}$) layer. (c) μBLS spectra measured using 100 ns voltage pulses with different amplitudes. The peak frequency of the AO mode is indicated by the markers in cyan.

induce injection locking of the AOs to the external radio frequency (rf) stimuli.

Figure 1(b) highlights the direction of the magnetic field and current needed for efficient generation of AOs by means of SHE and SOT [4,5,11]. In particular, the direction of the injected current (I), the polarization of the pure spin current (P) arising due to SHE and the direction of the magnetic moment (m) in the presence of an in-plane magnetic field (H). The external magnetic field should be applied in the direction perpendicular to the current flow, as the SOT efficiency is maximized [6,11,14]. At sufficiently large current densities and upon an appropriate choice of field polarity, this leads to damping compensation and consequent emergence of AOs in the constriction region. In the present experiments, H is tilted by 80° with regard to I, so that the fieldlike torque induced by the microwave current in the Pt layer has a component orthogonal to m. This results in an increased coupling between the AOs and the external microwave field, with little impact on the AOs [28,29]. In all experiments reported, the magnitude of H is first increased to 200 mT for the purpose of saturating the magnetization, and then decreased to 20 mT.

Time-resolved Brillouin light scattering microscopy (TR μBLS) is employed to measure the frequency spectra of the AOs as a function of time. Using this stroboscopic technique, nanosecond time resolution and submicron spatial resolution can be achieved [30]. The measurement apparatus includes electrical inputs for injecting voltage pulses and rf signals, generated by an arbitrary waveform generator and microwave source, combined via a microwave diplexer. The voltage pulses have a trapezoidal shape, with rise and fall times set to 4 ns and a repetition rate of 4 MHz.

II. MAGNETIZATION AUTO-OSCILLATIONS DRIVEN BY VOLTAGE PULSES

Figure 1(c) shows the BLS spectra as a function of V_p obtained using 100 ns pulses. The pulse amplitude is varied from 0.8 to 1.8 V. The AO frequency f_{AO} is varied from 3.1 to 2.2 GHz with increasing pulse amplitude. Such a frequency downshift is consistent with theory and with previous experiments involving SHNOs with a similar geometry [6,14,31]. The largest BLS signals are obtained in the voltage range 1.2–1.4 V.

Figure 2(a) shows the frequency-integrated μBLS spectra obtained using 100 ns voltage pulses at different amplitudes. The time dependence of the voltage pulse, measured using an oscilloscope, is plotted together using the vertical axis on the right. In order to compare the response time of the AOs with that of the voltage pulse, the onset and outset segments are fitted using a logistic function of the type $A_0(1 + e^{-\beta(t-t_0)})^{-1}$, where A_0 is the amplitude, β is an effective growth (decrease) rate and t_0 is the time at which half-amplitude ($A_0/2$) is reached [32]. In Fig. 2(a), the black lines at the onset and outset segments of the μBLS data correspond to the fitted function. The onset and outset segments of the voltage pulse are indicated by the fitting lines in red and gray and the vertical dashed lines indicate the t_0 of each segment. The parameter β is plotted in Fig. 2(b) and the difference between t_0 of the AO signal and

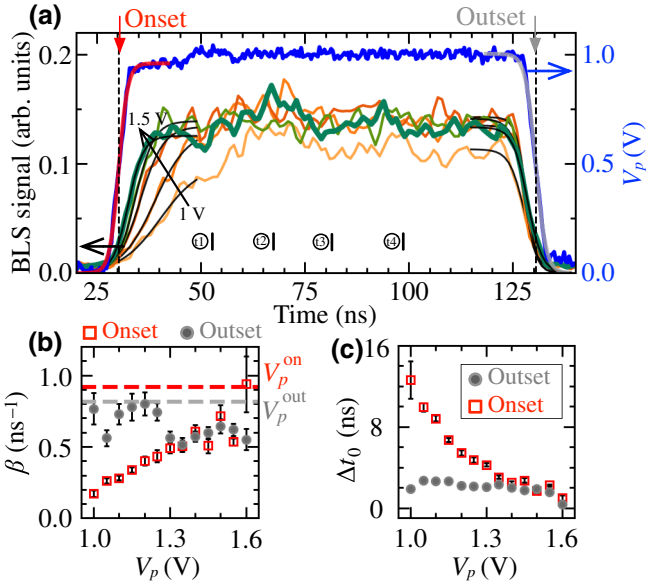

FIG. 2. (a) Frequency-integrated TR-μBLS signal obtained at different values of V_p between 1 and 1.5 V. The time dependence of V_p is included using the right axis. (b) Parameter $|\beta|$ at the onset and outset segments of the μBLS signal at different voltage values. Dashed lines show the $|\beta|$ of V_p. (c) The difference Δt_0 between t_0 of V_p and that of the μBLS signal at the onset (squares) and outset (circles) segments. Error bars show the standard deviation.

the voltage pulse at the onset (squares) and outset (circles) segments is shown in Fig. 2(c) (for further information, see the Supplemental Material [33]).

First, we note in Fig. 2(a) that the time dependence of the AO signal at the onset segment exhibits distinct time dependence with pulse amplitude while the outset segment remains approximately the same. As shown in Fig. 2(b), the onset growth rate of the AO is small for low voltages but increases at larger pulse amplitudes, approaching the rate of the voltage pulse. In contrast, the decrease rate of the outset segment remains approximately unchanged. At larger pulse amplitudes, the rates at the onset and outset are similar in magnitude. At the same time, the difference between the t_0 of the AO signal and voltage pulse at the onset segment decreases from 14 ns, at 1 V, to nearly zero at 1.6 V, while the time difference at the outset segment remains constant at about 2 ns, as shown in Fig. 2(c).

In the time segment between the onset and the outset, the integrated μBLS amplitude is not constant in time. Some representative time steps, where changes in the integrated μBLS signal are observed, appear, labeled t1–t4 in Fig. 2. The positions of t1–t4 appear to be irrespective of the pulse amplitude. In order to better understand the origin of these changes in the AO amplitude, we discuss the time dependence of the μBLS spectra.

Figure 3(a) shows the time dependence of the μBLS spectra obtained using 100 ns pulses with an amplitude of 1.4 V. At the onset segment of the AO signal, indicated by the vertical dashed line, we see a rapid increase in the AO amplitude, consistent with the data shown in Fig. 2(a), together with a reduction in the frequency from 2.95 to 2.65 GHz. The decrease in frequency can be explained based on the data of Fig. 1(c), where we see that the AO frequency decreases with increasing pulse amplitude. The rapid increase (decrease) in the frequency (amplitude) observed at the outset segment of the AO signal can be explained in the same manner.

The time segments t1–t4, also highlighted in Fig. 2(a), correspond to the time steps where changes in the AO frequency are observed. Note, for instance, the clear reduction in the AO frequency at approximately 72 ns. Above $t >$ t4 the AO frequency and amplitude appear to have reached a steady state.

Since the variations in the amplitude and frequency of the μBLS signal at t1–t4 appear to be independent of the pulse amplitude and pulse duration, we anticipate that these have origin in the instantaneous voltage pulse changes driving the AOs. The time dependence of the voltage pulse, presented in Fig. 2(a), shows that the local maximum of the voltage at the onset segment is about 5% lower than the maximum (nominal) voltage at the outset segment. In addition, between 50 and 70 ns the instantaneous voltage exhibits an undershoot and an overshoot of 6% and 4%, respectively, before it reaches a steady state above 70 ns. Such behavior is reminiscent of the ringing effect in an *RLC*-equivalent circuit as response to sudden changes in the input signal, namely at the onset. This can in part explain the oscillations in the amplitude following the AO onset.

With the exception of the onset and outset segments and despite the changes in the AO frequency, the linewidth remains approximately constant at 150 ± 2 MHz, throughout the whole pulse duration. However, rather than corresponding to the real AO linewidth, this value is consistent with the limit in resolution of the method employed. Electrical measurements of the AOs are carried out in a similar SHNO geometry using direct currents (not discussed here), where linewidths of 20 to 30 MHz are obtained. In our experiments, changes in the linewidth, or coherence, of the AOs are only observed at the onset and outset segments, while accompanied by frequency shifts, suggesting that the nanoconstriction SHNOs are agile down to the nanosecond timescale. A similar agility timescale is observed in spin torque nano-oscillator geometries [34,35] and nonlocal spin-injection spin valves [19].

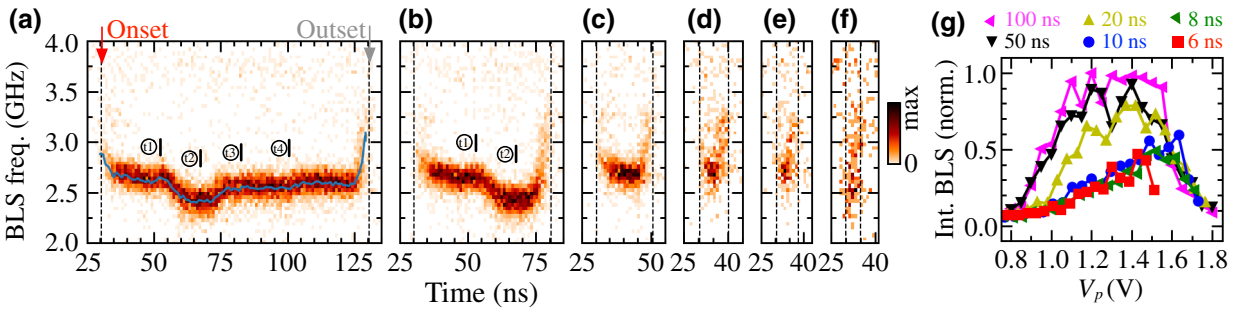

FIG. 3. (a)–(f) TR-μBLS spectra obtained at 1.4 V for pulse durations 100, 50, 20, 10, 8, and 6 ns. The continuous line in blue highlights the peak frequency as a function of time, obtained by fitting each time step using a Lorentzian function (see the Supplemental Material [33]). (g) Frequency-and-time-integrated μBLS signal plotted as a function of V_p for the various pulse durations. Signal integrated between 1.8 and 7.1 GHz, over the pulse width and normalized with respect to the signal obtained using 100 ns pulses.

The TR-μBLS data obtained using shorter pulses [Figs. 3(b)–3(f)] exhibit behavior similar to that described for the 100 ns pulses, especially the variation of the AO frequency at the onset and outset segments. In the case of shorter pulses, the TR-μBLS spectra between the onset and outset segments are simply truncated at the corresponding pulse duration. A noticeable difference is the decrease in the AO amplitude with decreasing pulse width, which is indicated by a change in color contrast in Figs. 3(a)–3(f). This can be better understood in Fig. 3(g), where we show the frequency-and-time-integrated μBLS signal, as a function of the pulse amplitude. For voltage pulses with durations of 10, 8, and 6 ns, one is unable to reach the same AO amplitude as for longer pulses, as shown by the 50% reduction in the integrated signal, compared to that obtained with 100 ns pulses. Since the onset and outset times are independent of the pulse duration, for shorter pulses, the time segment during which the nominal voltage is applied is very short. Therefore, the average amplitude per unit of time will be smaller compared to that of longer pulses. In order to increase the AO amplitude whilst applying pulses of a few nanoseconds, larger voltage amplitudes would be necessary. We note that the use of short pulses comes with the disadvantage of having a spreading of the frequency over the short existence of the AO signal due to the rise and fall of the amplitude at the onset and outset segments. A demonstration of the SHNO response while driven by a train of short voltage pulses is presented in the Supplemental Material [33].

Next, we discuss the agility of SHNOs in the case where microwave pulses are utilized as a frequency lock to the AO signal generated by voltage pulses.

III. INJECTION LOCKING USING MICROWAVE PULSES

In conventional injection-locking experiments, a magnetic field and a direct current are applied to the SHNO together with the external continuous-wave (CW) rf signal that couples to the AOs [28,36,37]. If the frequency of the rf signal, f, is close to either the natural AO frequency, f_{AO}, or $2f_{AO}$, the external rf stimuli pulls the AO frequency toward its own frequency (or $f/2$). This effect is observed over a range of frequencies surrounding f_{AO}, namely the injection-locking range, which can reach several hundreds of megahertz, depending on parameters such as the magnetic field strength, applied direct current and microwave power [28,36,37]. Injection locking is also known to result in a larger AO amplitude [29,38,39].

In the present manuscript, we create the conditions for injection locking to occur, except that instead of the direct current and CW-rf signals we apply voltage and rf pulses. The μBLS data shown in Fig. 4 are obtained while applying 150 ns wide rf pulses to the SHNO (at $t = 0$ ns) combined with 100 ns wide voltage pulses applied (at $t = 25$ ns). The inset plot in Fig. 4(a) shows the time dependence of the applied voltage and the rf pulse. The nominal voltage V_p is set to 1 V, and the frequency (f) of the rf pulses is varied from 5.4 to 6.8 GHz ($f \sim 2f_{AO}$) with a constant nominal rf power of 1 dBm. Compared to the injection locking obtained when $f \sim f_{AO}$, the frequency regime of $f \sim 2f_{AO}$ exhibited a wider frequency locking range and larger AO amplitudes, so only this case is discussed.

In Fig. 4(a), the frequencies corresponding to $f/2$ are illustrated by the diagonal dashed line. For values of $f/2$ well below 2.85 GHz, the frequency of the AO signal is constant, at f_{AO}. When $f/2 \sim 2.9$ GHz, we observe a down shift of the AO frequency, simultaneously with an increase in the AO amplitude, indicating the beginning of the synchronization to the external source, or the so-called injection-locking effect [28]. Large amplitude AOs remain as $f/2$ increases to 3.25 GHz. Above this frequency value, the AO amplitude decreases, and f_{AO} is gradually recovered. In these measurements, we obtained a frequency locking range of approximately 350 MHz.

Figure 4(b) shows the TR-μBLS spectra obtained at the indicated $f/2$ values of rf_p. The vertical dashed lines indicate the onset and outset times of V_p [from Fig. 2(a)]. The AO signal obtained at 2.73 GHz illustrates the limit of $f/2 < f_{AO}$. The spectra exhibit a weak AO mode at 3.0 GHz, whose amplitude is not evenly distributed within the duration of the voltage pulse. The time-varying AO amplitude seen here is consistent with the results discussed in Fig. 2(a).

The TR-μBLS spectra obtained for $f/2$ values of 2.95 and 3 GHz fall within the frequency locking range. It can be seen that the AO frequency and amplitude remain nearly constant within the duration of the voltage pulse, especially if compared to the rapid changes of the AO frequency observed earlier in Fig. 3(a). In the example corresponding to 3.3 GHz the injection-locking efficiency decreases as $f/2 > f_{AO}$. Here, the time dependence of the natural AO mode is partially restored, at 3.04 GHz.

Figure 4(c) shows the frequency-integrated μBLS signal resulting from the data shown in Fig. 4(b). The AO amplitude is nearly constant in the signals at 2.95 and 3.0 GHz and the growth rate increases significantly at these two frequencies. Here, a short AO rise time of 6 ns is obtained, while the temporal profile at 1 V shown in Fig. 2(a) (rf is *off*) exhibits a rise time of nearly 25 ns. This increase in the growth rate demonstrates that injection locking to an external signal with known frequency and phase contributes to an increase in the coherence of the AO signals. Despite the voltage oscillations inherent to the ringing effect of the input circuit, the AO signal remains stable within the pulse duration, which further demonstrates that improvements in the agility of the SHNO are achieved by means of injection locking.

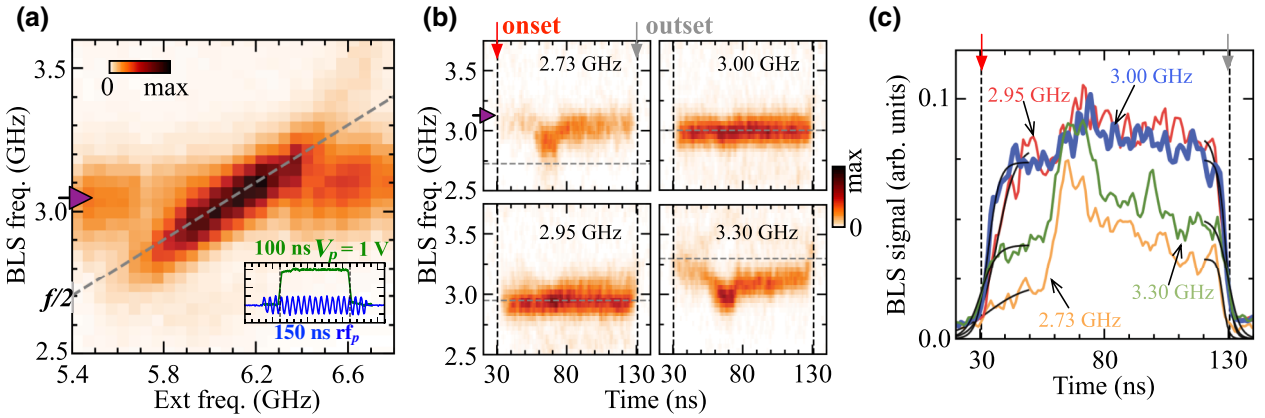

FIG. 4. (a) μBLS spectra as a function of the external rf frequency (f) obtained using 150 ns wide rf pulses (at $t = 0$ ns), followed by a 100 ns wide voltage pulse (at $t = 25$ ns), as shown in the inset plot (rf power 1 dBm). The diagonal line indicates the values of $f/2$. The arrow in magenta indicates f_{AO} [same as in (b)]. (b) TR-μBLS spectra at the $f/2$ values of rf$_p$, also indicated by horizontal dashed lines. The vertical dashed lines indicate the onset and outset of the voltage pulse. The color-coded intensity is normalized to a common value. (c) Frequency-integrated TR-μBLS signal (rf power 1 dBm), obtained from the data shown in (b).

The results discussed so far suggest the possibility to combine voltage and microwave pulses, which could give rise to a variety of AO amplitude patterns. In Fig. 5 we demonstrate two ways in which the voltage and rf inputs can be combined in order to generate short time segments with well-defined levels of AO amplitude.

In the approach discussed with Figs. 5(a)–5(e), voltage pulses with a duration of 125 ns ($V_p = 1$ V) are applied to the SHNO. Following the onset of the AO signal, we apply a sequence of three rf pulses, with 28 ns width and a separation of 15 ns. The time dependence of the input stimuli is shown in Fig. 5(a), where the vertical dashed lines coincide with the onset and outset of each rf pulse. Figure 5(b) shows the TR-μBLS spectra of the natural AO mode, obtained with the rf pulses switched off. Here, the oscillations in the AO frequency and the uneven distribution of the AO amplitude in the time domain are consistent with the ringing behavior of the AO signal, discussed in Fig. 3.

The TR-μBLS spectra of the pulsed injection-locking sequence are shown in Figs. 5(c) and 5(d) for $f/2$ values of 2.9 and 3.05 GHz, respectively, chosen within the frequency locking range of the measured device. As expected, injection locking occurs only during the three time segments coincident with the rf pulses. For the other two segments, where the rf excitation is switched off, the AO amplitude is considerably reduced as the natural AO frequency is restored.

Figure 5(e) shows the μBLS signals integrated between 2.6 and 3.5 GHz, obtained from the data shown in Figs. 5(b)–5(d). The frequency range of the integration (df) is illustrated by the horizontal lines. First, note that by applying the first rf pulse immediately after the onset of the AOs, the instantaneous amplitude increases such that the time profile of the AO amplitude becomes similar to that of the input voltage pulse [Fig. 5(a)], as a result of the increased growth rate. The two rf pulses that follow result in twice the AO amplitude compared to the natural AO mode. Using this approach, we obtain an amplitude-modulated AO signal, reminiscent of a two-level system alternating between the frequency-locked state (1) and the natural AO state (0.5).

Next, we discuss a method that allows us to obtain amplitude modulation of two frequencies at distinct time segments of a voltage pulse train. The voltage levels of the pulse train alternate between 1 and 0.5 V, as shown in Fig. 5(f). Here, the line in green corresponds to the trapezoidal pulses with a duration of 12 ns and a period of 30 ns, while the line in orange shows the voltage pulses combined with a CW-rf signal.

The TR-μBLS spectra obtained when applying the voltage pulses only (rf is off) is shown in Fig. 5(g), where we note that the AO mode appears at 2.95 GHz, in the time segments where the instantaneous voltage is equal to V_p. Here, the frequency upshift observed at the onset and outset of the AO signal is coincident with the time segments corresponding to the rise and fall of the voltage pulses. In the time segments coincident with $V_p/2 = 0.5$ V, the AO signal is too small to be detected. This is expected since we learned from the results presented in Fig. 1(c) that below 0.8 V the AO signal is weak.

When the CW-rf signal is switched on, at $f/2 =$ 2.8 GHz, injection locking is observed, as shown in Fig. 5(h), where the resulting AOs have larger amplitude compared to the natural AO signal. It is worth noting that the frequency upshift observed in Fig. 5(g) is suppressed due to injection locking. Despite the improved frequency stability of the AO signal, no signal is detected in the time segments coincident with $V_p/2$.

Interestingly, when the frequency of the CW-rf signal is larger than f_{AO}, as in the example shown in Fig. 5(i), a

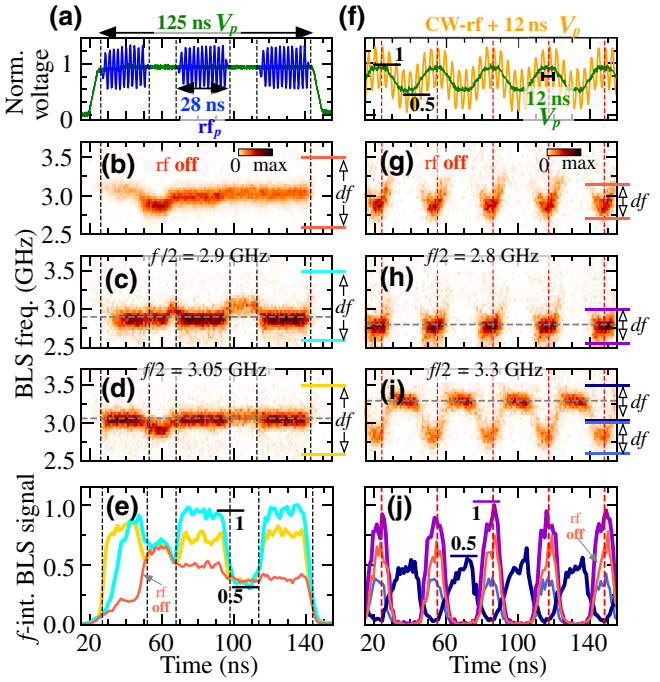

FIG. 5. (a) Time dependence of V_p (green) and the rf pulses (blue). (b) TR-μBLS spectra measured while applying $V_p = 1$ V only (rf off). (c) and (d) TR-μBLS spectra obtained while applying V_p (1 V) and rf pulse trains with the indicated $f/2$ values (rf power of 1 dBm). Color-coded μBLS intensities of (b)–(d) are normalized to the same value. (e) The TR-μBLS intensities of (b; orange), (c; cyan), and (d; yellow) integrated from 2.6 to 3.5 GHz, as indicated by the vertical arrows labeled *df* . (f) Time dependence of V_p with (orange) and without (green) an added CW-rf signal. (g) TR-μBLS spectra measured while applying the voltage train only (rf off). (h),(i) TR-μBLS spectra obtained at two different $f/2$ values, within the injection-locking range (rf power of 1 dBm). Color-coded intensities of (g)–(i) are normalized to the same value. (j) Frequency-integrated TR-μBLS signal showing the AO amplitudes obtained from (g; orange), (h; purple), (i; light blue), and the spin wave amplitude (dark blue). The frequency integration ranges are illustrated by the vertical arrows on the right.

μBLS signal is observed at $f/2 = 3.3$ GHz, in the time segments coincident with the $V_p/2$ level, while in the time segments coincident with the V_p level, the natural AO mode at f_{AO} is observed.

The observation of the μBLS signal in the time segments coincident with $V_p/2$ may be interpreted in the following manner. While the pure spin current in the $V_p/2$ level may not be sufficient to fully compensate the damping and efficiently generate AOs, it still contributes to a decrease in the effective damping. In this scenario, a down shift of the spin wave band in the constriction region is expected, owing to partial damping compensation. As a consequence, when applying rf pulses with $f > f_{AO}$, one is able to directly excite and detect spin waves.

Figure 5(j) shows the TR-μBLS signal integrated over a 450 MHz frequency range surrounding the detected spin waves and the AO frequency, as illustrated by the horizontal lines in Figs. 5(g)–5(i). The data show two modes corresponding to V_p and $V_p/2$, obtained at two distinct time segments of the duty cycle. These two signals differ in frequency by 0.5 GHz, as a result of the two different external rf frequencies and the natural AO frequency.

IV. CONCLUSION

Using a single magnetic oscillator, we generate nanosecond wide AO signals in the gigahertz frequency regime, under pulsed operation. We observe changes in the agility or growth rate of the AOs with the pulse amplitude. This increase in agility with increasing voltage is expected in nonlinear systems [6,19], as is the case of the damping compensation process by involving SHE and SOT. Rise times of about 6 ns for the auto-oscillations are obtained. This value is consistent with the rise time of the voltage pulse and not an intrinsic limit of the SHNOs. Moreover, the fact that we observe the response time of the circuit in the form of time-varying AO frequencies demonstrates that AOs could follow the rapid changes in the instantaneous voltage of the input stimuli, at least within the nanosecond time resolution of TR μBLS.

The injection-locking experiments show that the coupling of the SHNO to external microwave pulses results in improved temporal agility and a more stable output signal. A transition time of 6 ns is obtained from "0" to "1" states, even for low voltage amplitudes.

The control over the frequency and amplitude of magnetic oscillators with nanosecond time resolution is important for applications. There exist a number of approaches via which the oscillation frequency can be controlled, for example, via changing the amplitude and polarity of the direct current [40] or the external magnetic field, injection locking, and voltage control [41]. The present results suggest that such approaches may also work efficiently when operating with nanosecond voltage pulses. The tunability over the frequency and amplitude of the magnetic oscillators, gained when combining pulsed voltage and injection locking, can be viewed as demonstration of amplitude and frequency shift keying using nanoconstriction SHNOs. While this is conceptually similar to what was proposed using nanopillar structures [34,42–44], the SHNO geometry can be advantageous due to an easier fabrication, the ability to emit spin waves and the possibility to reach long-range synchronization. Further understanding of the ability to sweep the frequency using voltage pulses, without significant changes in the linewidth and amplitude, could allow fast spectral analysis [18] at the gigahertz frequency range, using nanoconstriction-based SHNOs.

ACKNOWLEDGMENTS

Financial support by the Deutsche Forschungsgemeinschaft is gratefully acknowledged within program

SCHU2922/1-1. Support by the Nanofabrication Facilities Rossendorf (NanoFaRo) at the IBC is gratefully acknowledged.

[1] G. Csaba and W. Porod, Coupled oscillators for computing: A review and perspective, Appl. Phys. Rev. **7**, 011302 (2020).
[2] D. Marković, A. Mizrahi, D. Querlioz, and J. Grollier, Physics for neuromorphic computing, Nat. Rev. Phys. **2**, 499 (2020).
[3] B. Dieny, *et al.*, Opportunities and challenges for spintronics in the microelectronics industry, Nat. Electron. **3**, 446 (2020).
[4] J. Slonczewski, Current-driven excitation of magnetic multilayers, J. Magn. Magn. Mater. **159**, L1 (1996).
[5] L. Berger, Emission of spin waves by a magnetic multilayer traversed by a current, Phys. Rev. B **54**, 9353 (1996).
[6] A. Slavin and V. Tiberkevich, Nonlinear auto-oscillator theory of microwave generation by spin-polarized current, IEEE Trans. Magn. **45**, 1875 (2009).
[7] L. Liu, C.-F. Pai, D. C. Ralph, and R. A. Buhrman, Magnetic Oscillations Driven by the Spin Hall Effect in 3-Terminal Magnetic Tunnel Junction Devices, Phys. Rev. Lett. **109**, 186602 (2012).
[8] T. Chen, R. K. Dumas, A. Eklund, P. K. Muduli, A. Houshang, A. A. Awad, P. Dürrenfeld, B. G. Malm, A. Rusu, and J. Åkerman, Spin-torque and spin-hall nano-oscillators, Proc. of the IEEE **104**, 1919 (2016).
[9] M. Dyakonov and V. Perel, Current-induced spin orientation of electrons in semiconductors, Phys. Lett. A **35**, 459 (1971).
[10] J. E. Hirsch, Spin Hall Effect, Phys. Rev. Lett. **83**, 1834 (1999).
[11] K. Ando, S. Takahashi, K. Harii, K. Sasage, J. Ieda, S. Maekawa, and E. Saitoh, Electric Manipulation of Spin Relaxation Using the Spin Hall Effect, Phys. Rev. Lett. **101**, 1 (2008).
[12] A. Hoffmann, Spin hall effects in metals, IEEE Trans. Magn. **49**, 5172 (2013).
[13] J. Sinova, S. O. Valenzuela, J. Wunderlich, C. H. Back, and T. Jungwirth, Spin hall effects, Rev. Mod. Phys. **87**, 1213 (2015).
[14] V. E. Demidov, S. Urazhdin, A. Zholud, A. V. Sadovnikov, and S. O. Demokritov, Nanoconstriction-based spin-hall nano-oscillator, Appl. Phys. Lett. **105**, 172410 (2014).
[15] B. Divinskiy, V. E. Demidov, S. Urazhdin, R. Freeman, A. B. Rinkevich, and S. O. Demokritov, Excitation and amplification of spin waves by spin-orbit torque, Adv. Mater. **30**, 1802837 (2018).
[16] M. Dvornik, A. A. Awad, and J. Åkerman, Origin of Magnetization Auto-Oscillations in Constriction-Based Spin Hall Nano-Oscillators, Phys. Rev. Appl. **9**, 014017 (2018).
[17] S. Louis, O. Sulymenko, V. Tiberkevich, J. Li, D. Aloi, O. Prokopenko, I. Krivorotov, E. Bankowski, T. Meitzler, and A. Slavin, Ultra-fast wide band spectrum analyzer based on a rapidly tuned spin-torque nano-oscillator, Appl. Phys. Lett. **113**, 112401 (2018).
[18] A. Litvinenko, V. Iurchuk, P. Sethi, S. Louis, V. Tyberkevych, J. Li, A. Jenkins, R. Ferreira, B. Dieny, A. Slavin, and U. Ebels, Ultrafast sweep-tuned spectrum analyzer with temporal resolution based on a spin-torque nano-oscillator, Nano Lett. **20**, 6104 (2020).
[19] B. Divinskiy, V. E. Demidov, S. O. Demokritov, A. B. Rinkevich, and S. Urazhdin, Route toward high-speed nano-magnonics provided by pure spin currents, Appl. Phys. Lett. **109**, 252401 (2016).
[20] V. E. Demidov, S. Urazhdin, G. de Loubens, O. Klein, V. Cros, A. Anane, and S. O. Demokritov, Magnetization oscillations and waves driven by pure spin currents, Phys. Rep. **673**, 1 (2017).
[21] S. Kaka, M. R. Pufall, W. H. Rippard, T. J. Silva, S. E. Russek, and J. A. Katine, Mutual phase-locking of microwave spin torque nano-oscillators, Nature **437**, 389 (2005).
[22] S. Sani, J. Persson, S. Mohseni, Y. Pogoryelov, P. Muduli, A. Eklund, G. Malm, M. Käll, A. Dmitriev, and J. Åkerman, Mutually synchronized bottom-up multi-nanocontact spin–torque oscillators, Nat. Commun. **4**, 2731 (2013).
[23] A. A. Awad, P. Dürrenfeld, A. Houshang, M. Dvornik, E. Iacocca, R. K. Dumas, and J. Åkerman, Long-range mutual synchronization of spin Hall nano-oscillators, Nat. Phys. **13**, 292 (2017).
[24] M. Romera, P. Talatchian, S. Tsunegi, F. Abreu Araujo, V. Cros, P. Bortolotti, J. Trastoy, K. Yakushiji, A. Fukushima, H. Kubota, S. Yuasa, M. Ernoult, D. Vodenicarevic, T. Hirtzlin, N. Locatelli, D. Querlioz, and J. Grollier, Vowel recognition with four coupled spin-torque nano-oscillators, Nature **563**, 230 (2018).
[25] M. Zahedinejad, A. A. Awad, S. Muralidhar, R. Khymyn, H. Fulara, H. Mazraati, M. Dvornik, and J. Åkerman, Two-dimensional mutually synchronized spin Hall nano-oscillator arrays for neuromorphic computing, Nat. Nanotechnol. **15**, 47 (2020).
[26] J. Torrejon, M. Riou, F. A. Araujo, S. Tsunegi, G. Khalsa, D. Querlioz, P. Bortolotti, V. Cros, K. Yakushiji, A. Fukushima, H. Kubota, S. Yuasa, M. D. Stiles, and J. Grollier, Neuromorphic computing with nanoscale spintronic oscillators, Nature **547**, 428 (2017).
[27] M. Riou, F. Abreu Araujo, J. Torrejon, S. Tsunegi, G. Khalsa, D. Querlioz, P. Bortolotti, V. Cros, K. Yakushiji, A. Fukushima, H. Kubota, S. Yuasa, M. D. Stiles, and J. Grollier, Neuromorphic computing through time-multiplexing with a spin-torque nano-oscillator, Technical Digest - International Electron Devices Meeting, IEDM, 36.3.1 (2018).
[28] V. E. Demidov, H. Ulrichs, S. V. Gurevich, S. O. Demokritov, V. S. Tiberkevich, A. N. Slavin, A. Zholud, and S. Urazhdin, Synchronization of spin Hall nano-oscillators to external microwave signals, Nat. Commun. **5**, 3179 (2014).
[29] T. Hache, T. Weinhold, K. Schultheiss, J. Stigloher, F. Vilsmeier, C. Back, S. S. P. K. Arekapudi, O. Hellwig, J. Fassbender, and H. Schultheiss, Combined frequency and time domain measurements on injection-locked, constriction-based spin Hall nano-oscillators, Appl. Phys. Lett. **114**, 102403 (2019).
[30] T. Sebastian, K. Schultheiss, B. Obry, B. Hillebrands, and H. Schultheiss, Micro-focused brillouin light scattering:

Imaging spin waves at the nanoscale, Front. Phys. **3**, 1 (2015).

[31] H. Mazraati, S. R. Etesami, S. A. H. Banuazizi, S. Chung, A. Houshang, A. A. Awad, M. Dvornik, and J. Åkerman, Auto-Oscillating Spin-Wave Modes of Constriction-Based Spin Hall Nano-Oscillators in Weak In-Plane Fields, Phys. Rev. Appl. **10**, 1 (2018).

[32] W. Rippard, M. Pufall, and A. Kos, Time required to injection-lock spin torque nanoscale oscillators, Appl. Phys. Lett. **103**, 182403 (2013).

[33] See Supplemental Material at http://link.aps.org/supplemental/10.1103/PhysRevApplied.16.054050 for more information on the fitting results pertaining to the TR-μBLS data shown in Secs. II and III, and further demonstration of the use of voltage and microwave pulses to obtain amplitude and frequency modulation of the microwave output of SHNOs.

[34] M. Manfrini, T. Devolder, J. V. Kim, P. Crozat, N. Zerounian, C. Chappert, W. Van Roy, L. Lagae, G. Hrkac, and T. Schrefl, Agility of vortex-based nanocontact spin torque oscillators, Appl. Phys. Lett. **95**, 1 (2009).

[35] T. Taniguchi, T. Ito, S. Tsunegi, H. Kubota, and Y. Utsumi, Relaxation time and critical slowing down of a spin-torque oscillator, Phys. Rev. B **96**, 1 (2017).

[36] S. Urazhdin, V. Tiberkevich, and A. Slavin, Parametric Excitation of a Magnetic Nanocontact by a Microwave Field, Phys. Rev. Lett. **105**, 1 (2010).

[37] E. Jué, M. R. Pufall, and W. H. Rippard, Asymmetric and partial injection locking of a three-terminal spin-torque oscillator, Appl. Phys. Lett. **112**, 00 (2018).

[38] K. Wagner, A. Smith, T. Hache, J.-R. Chen, L. Yang, E. Montoya, K. Schultheiss, J. Lindner, J. Fassbender, I. Krivorotov, and H. Schultheiss, Injection locking of multiple auto-oscillation modes in a tapered nanowire spin Hall oscillator, Sci. Rep. **8**, 16040 (2018).

[39] T. Hache, M. Vaňatka, L. Flajšman, T. Weinhold, T. Hula, O. Ciubotariu, M. Albrecht, B. Arkook, I. Barsukov, L. Fallarino, O. Hellwig, J. Fassbender, M. Urbánek, and H. Schultheiss, Freestanding Positionable Microwave-Antenna Device for Magneto-Optical Spectroscopy Experiments, Phys. Rev. Appl. **13**, 054009 (2020).

[40] T. Hache, Y. Li, T. Weinhold, B. Scheumann, F. J. T. Gonçalves, O. Hellwig, J. Fassbender, and H. Schultheiss, Bipolar spin Hall nano-oscillators, Appl. Phys. Lett. **116**, 192405 (2020).

[41] H. Fulara, M. Zahedinejad, R. Khymyn, M. Dvornik, S. Fukami, S. Kanai, H. Ohno, and J. Åkerman, Giant voltage-controlled modulation of spin Hall nano-oscillator damping, Nat. Commun. **11**, 4006 (2020).

[42] H. S. Choi, S. Y. Kang, S. J. Cho, I. Y. Oh, M. Shin, H. Park, C. Jang, B. C. Min, S. I. Kim, S. Y. Park, and C. S. Park, Spin nano-oscillator-based wireless communication, Sci. Rep. **4**, 1 (2014).

[43] R. Sharma, P. Dürrenfeld, M. Ranjbar, R. K. Dumas, J. Akerman, and P. K. Muduli, Modulation rate study in a spin-torque oscillator-based wireless communication system, IEEE Trans. Magn. **51**, 11 (2015).

[44] A. Ruiz-Calaforra, A. Purbawati, T. Brächer, J. Hem, C. Murapaka, E. Jiménez, D. Mauri, A. Zeltser, J. A. Katine, M. C. Cyrille, L. D. Buda-Prejbeanu, and U. Ebels, Frequency shift keying by current modulation in a MTJ-based STNO with high data rate, Appl. Phys. Lett. **111**, 1 (2017).